Regular and chaotic motions of the fast rotating rigid body: a numerical study

Giancarlo Benettin[*] Anna Maria Cherubini[†] Francesco Fassò[‡]

(Revised version – March 12, 2002)

Abstract

We numerically investigate the dynamics of a symmetric rigid body with a fixed point in a small analytic external potential (equivalently, a fast rotating body in a given external field) in the light of previous theoretical investigations based on Nekhoroshev theory. Special attention is posed on "resonant" motions, for which the tip of the unit vector μ in the direction of the angular momentum vector can wander, for no matter how small ε, on an extended, essentially two–dimensional, region of the unit sphere, a phenomenon called "slow chaos". We produce numerical evidence that slow chaos actually takes place in simple cases, in agreement with the theoretical prediction. Chaos however disappears for motions near proper rotations around the symmetry axis, thus indicating that the theory of these phenomena still needs to be improved. An heuristic explanation is proposed.

1 Introduction

A. The purpose. In this paper we shall investigate the dynamics of the perturbed Euler–Poinsot rigid body, namely a rigid body with a fixed point in a small positional potential. The Hamiltonian has the form

$$\mathcal{H} = \mathcal{K} + \varepsilon \mathcal{V} \ , \tag{1.1}$$

where $\mathcal{K}$ is the kinetic energy; the potential $\mathcal{V}$ is assumed to depend only on the configuration of the body and to be regular, in fact analytic. The problem is equivalent to the problem of the fast rotating rigid body in a given (non small) potential $\mathcal{V}$: indeed the motions of Hamiltonian (1.1), for given initial data and small ε, are identical, up to a rescaling, to the motions of the same Hamiltonian with $\varepsilon = 1$ and large velocities, namely velocities rescaled by a factor $1/\sqrt{\varepsilon}$ (time needs also to be rescaled, by a factor $\sqrt{\varepsilon}$). The perturbed Euler–Poinsot rigid body was studied by Arnold in the context of KAM theory, in the case in which $\mathcal{V}$ has cylindrical symmetry, as it happens for a heavy rigid body. The case of a generic external potential was instead studied a few years ago in

[*]Università di Padova, Dipartimento di Matematica Pura e Applicata, INFM and GNFM, Via G. Belzoni 7, 35131 Padova, Italy (E–mail: benettin@math.unipd.it).

[†]Università di Lecce, Dipartimento di Matematica and GNFM, Via per Arnesano, 73100 Lecce, Italy (E–mail: anna.cherubini@unile.it).

[‡]Università di Padova, Dipartimento di Matematica Pura e Applicata and GNFM, Via G. Belzoni 7, 35131 Padova, Italy (E–mail: fasso@math.unipd.it).

[3] [4], in the context of Nekhoroshev theory.[1] In the very essence, in [3] and [4] it is proven that, for "nonresonant" initial data (see below for the notion) the motions of the rigid body are regular, while for "resonant" initial data chaotic motions are possible, more precisely the tip of the angular momentum m of the body can wander unpredictably on the sphere $\|m\| = \text{const}$. The aim of this paper is to investigate numerically the level of accuracy of the theory, that is, practically, to check whether chaotic motions are indeed present whenever the theory allows for their existence. As we shall see, the answer is not trivial: namely the correspondence between theory and numerical results is generically good, but there is a remarkable exception, namely "gyroscopic" motions (motions close to proper rotations) appear to be more stable than the theoretical expectation. This fact prompts for a deeper theoretical understanding, and we also give a contribution in this direction, by suggesting a possible way to improve the theory.

To be more precise, we need to recall very shortly the results of [3] and [4]. As there explained, the long–time properties of the motion of the perturbed system are strongly influenced by the "proper degeneracy", or "superintegrability", of the Euler–Poinsot system, namely the fact that the unperturbed Hamiltonian, even if it has three degrees of freedom, depends in fact only on two "nondegenerate" actions, and has only two independent frequencies. Let us consider, for simplicity, a symmetric body, with moments of inertia $I_1 = I_2 \neq I_3$, and denote by (O, e_1, e_2, e_3) a frame attached to the body, e_3 being the symmetry axis. For $\varepsilon = 0$ the body performs an Euler–Poinsot motion, namely m stays constant in space, while e_3 precedes regularly around it, $m \cdot e_3$ being constant. The two independent frequencies are precisely the components of the angular velocity of the body along m and along e_3 (the familiar frequencies of the rolling "Poinsot cones"), and depend only on $G = \|m\|$ and $L = m \cdot e_3$, which turn out to be the nondegenerate actions (see later); the two dimensional frequency vector turns out to be

$$\omega(G, L) = \frac{1}{I_1}(G, \eta L) \ , \qquad \eta = \frac{I_1}{I_3} - 1 \ . \tag{1.2}$$

The main results of [3] and [4] can be summarized as follows:

1) Up to an "exponentially large" time scale $t \sim \exp \varepsilon^{-1/4}$, G and L stay nearly constant, namely they oscillate at most by quantities of order $\sqrt{\varepsilon}$.
2) During this time, the body performs approximately (up to deviations of order $\sqrt{\varepsilon}$) an Euler–Poinsot motion around the istantaneous direction of the angular momentum m, with frequencies $\sqrt{\varepsilon}$–close to the initial ones; m however stays not fixed, but moves slowly in space, with speed of order ε.

In view of this, it is of central importance to understand the dynamics of m in space, on the long intermediate time scale $1/\varepsilon \ll t \ll \exp \varepsilon^{-1/4}$. It turns out that the behavior of m is essentially influenced by the resonance properties of the vector ω (which according to the above statements stay nearly constant during the exponential time scale). Precisely, denoting by μ the unit vector in the direction of m:

3.a) If ω is nonresonant (up to some low resonance order, see [13], [12]), then μ remains $\varepsilon^{1/4}$–near a level curve of a suitable regular function on the unit sphere, namely the average of the potential energy on the "fast angles" g and l canonically conjugated to G and L (figure 1a). So, up to times growing as $\exp \varepsilon^{-1/4}$, the motion of the system is essentially regular, consisting

[1] In such references, which are quite important for the present paper, the choice was $\varepsilon = 1$ and initial data with angular velocity of large norm Ω. Here we are using small ε only because, in this language, some relevant expressions are more immediately understood. Anyhow, translating formulae is always easy, by keeping in mind the correspondence $\Omega = 1/\sqrt{\varepsilon}$.

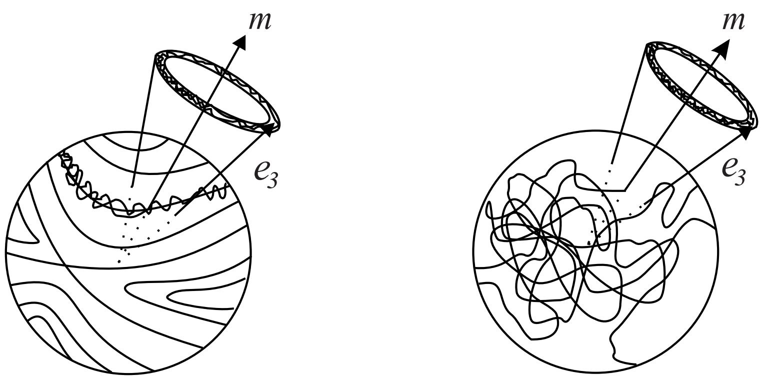

Figure 1: *Possible motions of $\mu = m/\|m\|$ on S^2: almost regular motion close to a level curve of the averaged potential energy (left); slow chaotic motion filling a two dimensional portion of S^2 (right). In both cases e_3 preceeds almost regularly about the instantaneous direction of m.*

of an approximate Euler–Poinsot precession around a certain direction, which in turn slowly advances along a well defined curve.

3.b) If instead ω is low resonant, then the above conclusion cannot be reached, and it might happen that the direction of m spreads unpredictably through an extended, essentially two–dimensional region on the unit sphere, which does not shrink to a curve for $\varepsilon \to 0$ (figure 1b). This "slow chaos" [7] takes place on times which are long compared with $1/\varepsilon$, but short compared with $\exp \varepsilon^{-1/4}$, and is different from Arnold diffusion, which consists in significant changes of G and L, and (possibly) takes place on an exponentially long time scale.

Properly speaking, the conclusion of [3] and [4] is that slow chaotic motions of m, for resonant initial data, are not forbidden. It is clearly important to study their actual existence in specific systems: if chaotic motions are typically found when they are theoretically allowed, with a good correspondence between presence of resonances and presence of chaos, then the rigid body dynamics should be considered, for this respect, essentially understood. In the opposite case, namely in lack of such a correspondence, the conclusion should be that the theoretical study still needs important improvements. The purpose of the present paper is to obtain some insight on this question, by numerically investigating some elementary examples. In short, our numerical computations suggest that:

i) For non–gyroscopic motions (that is, motions sufficiently far from proper rotations around the symmetry axis e_3) slow chaotic motions of m are indeed present in low resonances, even for simple potentials, and do not disappear by decreasing ε.

ii) On the contrary, slow chaos is not present, even in low resonances, for nearly gyroscopic motions. We made a special effort to detect gyroscopic chaotic motions in a few particularly promising low order resonances (see the theoretical analysis in Section 4), but we could never observe them: we found indeed several examples of chaotic motions in low resonances for not too small ε, but at variance with the non gyroscopic situation, they always disappeared by decreasing ε. So, *nearly gyroscopic motions appear to be substantially more regular than the theoretical expectation of* [4].

A better understanding of the gyroscopic case, beyond the analysis of [4] (and the improvements of [12]), seems to be necessary. We shall not fully enter here this theoretical question, which is delicate and requires a rather careful mathematical analysis, far beyond the scopes and the style of the present article. Nevertheless, we shall provide some theoretical insight on the problem, by pointing out a possibly important theoretical element, not considered in the previous papers, which could explain the special regularity of gyroscopic motions.

B. The numerical method. One delicate point in integrating the equations of motion of a rigid body is obviously related to the fact that its phase space $T^*\mathrm{SO}(3)$ is not an Euclidean space, but a manifold. Several methods have been developed for dealing with such a situation (see e.g. [8] for some of the early work using quaternions). In our case, since we are interested on long time integrations, symplectic methods such as RATTLE [16] [17] or some splitting method appear to be a natural choice. We found preferable to use the latter approach and performed all the numerical computations with the basic second order splitting algorithm

$$\Psi_\tau = \Phi^{\varepsilon\mathcal{V}}_{\tau/2} \circ \Phi^{\mathcal{K}}_{\tau} \circ \Phi^{\varepsilon\mathcal{V}}_{\tau/2} \ , \tag{1.3}$$

where τ is the time–step and $\Phi^{\mathcal{F}}_\tau$ is the map at time τ of the flow of the Hamiltonian vector field of a function $\mathcal{F}$. (See e.g. [23] [24] for general properties of splitting methods and for higher order algorithms).

In the case of a rigid body, the algorithm (1.3) can be implemented in a variety of ways. The more common implementation [22] [18] [19] relies on left trivialization of $T^*\mathrm{SO}(3)$ and leads to an algorithm for the angular momentum vector in the body and for the rotational matrix or, equivalently, for a unit quaternion. (See also [6] for the implementation details. In fact, all these works were focused on the case of an asymmetric body, which is treated by a further splitting of the Euler–Poinsot flow $\Phi^{\mathcal{K}}_\tau$). We adopted instead a different possibility, recently proposed in [1], which consists of implementing the algorithm in two local coordinate systems, which together form an atlas for $T^*\mathrm{SO}(3)$. Specifically, we cover $T^*\mathrm{SO}(3)$ with two charts of Euler coordinates (the usual Euler angles θ, ϕ, ψ and their conjugate momenta; such coordinates are more convenient than the action–angle ones for the numerical integration) and integrate the local representative of the map Ψ_τ in one chart, switching to the other as soon as a coordinate singularity is approached. Thanks to its SO(3) symmetry, the Euler–Poinsot flow Φ^K_τ is the same in both charts and, in the case considered here of a symmetric body, it can be computed exactly and efficiently (it requires only four trigonometric functions besides a number of algebraic operations). In each chart, the flow $\Phi^V_{\tau/2}$ is just a shift of the momenta. The details of the method can be found in [1].

However implemented, the method (1.3) is symplectic and explicit and appears to perform very well, with good stability and efficiency. Furthermore, as well as other symplectic integrators, including RATTLE [20] [21] [15], the method admits a global "interpolating Hamiltonian" (or "modified Hamiltonian") $\widetilde{\mathcal{H}}_\tau$, with the well known advantages on energy conservation, see [2] [14]. But in addition, the splitting method (1.3) has an important feature for the case at hand of a small perturbation of the Euler–Poinsot system. Indeed if, as we do, the Euler–Poinsot flow $\Phi^{\mathcal{K}}_\tau$ is computed exactly, then the local error of the algorithm is of order $\varepsilon\tau^3$ and the interpolating Hamiltonian $\widetilde{\mathcal{H}}_\tau$ differs from $\mathcal{H}$ at order $\varepsilon\tau^2$ (see [1] for details). This makes the algorithm especially useful in perturbation studies since the time–step needs not be decreased with ε.

2 Normal forms

Before presenting the numerical results, it is useful to introduce, very shortly, some theoretical elements concerning the rigid body dynamics, and review in particular a few geometrical aspects of the unperturbed motion, which turn out to be useful to understand the dynamics of the perturbed system. Here of course we limit ourselves only to the very essentials; for a wider discussion see the above quoted references, in particular [10].

A. The unperturbed system. Let us preliminarily recall, with the help of figure 2, the definition of the action–angle coordinates (G, L, J, g, l, j) of the unperturbed system. As already remarked, the nondegenerate actions G and L are respectively the length $\|m\|$ of the angular momentum and its component $m \cdot e_3$. The third "degenerate" action J is instead the component of m along the z–axis of an arbitrarily chosen frame (O, e_x, e_y, e_z), fixed in space. Concerning the angles, j is the angle from e_x to $n_1 = e_z \times m$, in the plane orthogonal to e_z; g is the angle from n_1 to $n_2 = e_3 \times m$, in the plane orthogonal to m; finally l is the angle from n_2 to e_1, in the plane orthogonal to e_3. Quite clearly, G, L and l are intrinsically defined, that is are independent of the choice of the spatial frame, while J, j depend in an essential way on it (they determine the orientation of m in that spatial frame); g also depends on the spatial frame, but so to speak only marginally, namely only for the choice of the origin. In the action–angle coordinates, the kinetic energy depends only on G and L, and is

$$\mathcal{K}(G, L) = \frac{1}{2I_1}\left(G^2 + \eta L^2\right) \ ;$$

the corresponding frequency vector is ω given in (1.2). The perturbed Hamiltonian $\mathcal{H}$ in turn has the form

$$\mathcal{H}(G, L, J, g, l, j) = \mathcal{K}(G, L) + \varepsilon \mathcal{V}(G, L, J, g, l, j) \ ,$$

$\mathcal{V}$ being homogeneous of degree zero in the actions.[2]

The action–angle coordinates are singular when $e_z \times m = 0$ or $m \times e_3 = 0$. These singularities, however, are of quite different nature, as is realized by looking carefully at the structure of the phase space of the rigid body as determined by the unperturbed dynamics. Exclude for a moment the singularity associated to proper rotations, i.e. restrict the attention to $M \subset T^*SO(3)$ such that $m \times e_3 \neq 0$. The structure of M is easily understood: the actions G and L are globally defined in M, and take values in the "action space" $A = \{(G, L) \in \mathbb{R}^2 : G > 0, |L| < G\}$. For each point (G, L) in A, the unit vector μ along the angular momentum runs on the two dimensional sphere S^2, and $(J/G, j)$ are local coordinates on it (this is the sphere apparing in figure 1). Finally, for each choice of $(G, L) \in A$ and of $\mu \in S^2$, the angles g and l run on a torus $\mathbb{T}^2$. Since l is intrinsic, while g is not so only for the origin, the torus turns out to be intrinsic, and to coincide with the set of fixed m and $m \cdot e_3$. For a dense subset of A, the frequency ω is non resonant, so the torus is the closure of unperturbed orbits starting on it, and cannot be further decomposed. In conclusion, M is naturally foliated into tori $\mathbb{T}^2$, the foliation being independent of the choice of the spatial frame.[3]

The singularity $e_z \times m = 0$ of the action–angle coordinates has no dynamical meaning, and simply expresses the fact that S^2 cannot be covered by a single chart of local coordinates: it is just

[2] $\mathcal{V}$ is homogeneous because the potential is positional. Thanks to this fact, the canonical scaling $G = G'\sqrt{\varepsilon}$, $L = L'\sqrt{\varepsilon}$, $J = J'\sqrt{\varepsilon}$, $t = t'/\sqrt{\varepsilon}$, conjugates H with H' of the same form, but with $\varepsilon = 1$.

[3] M has a double structure of fiber bundle: it is a fiber bundle with basis $A \times S^2$ and fiber $\mathbb{T}^2$, but it is also a fiber bundle with basis A and fiber F, which in turn is a fiber bundle with basis S^2 and fiber $\mathbb{T}^2$; F is precisely the collection of tori supporting motions with the same frequencies. Both structures are global and free of singularities in M. Instead the foliation in tori $\mathbb{T}^3$, as resulting from the Liouville–Arnold theorem, is only local, since it depends in an essential way on the spatial frame (it depends on the choice of the cylindrical–like coordinates J, j on the sphere, and is obtained by grouping together tori $\mathbb{T}^2$ with the same J, so as to form tori $\mathbb{T}^3$). A similar structure of double fibration is characteristic of all degenerate systems, see [9] [10].

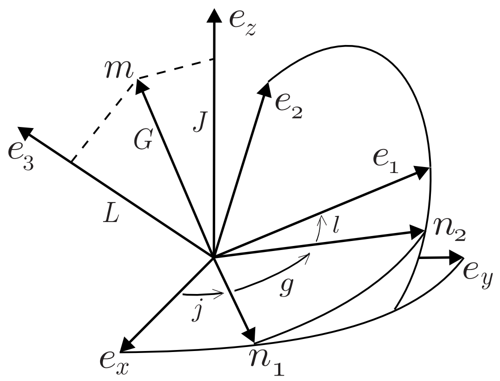

Figure 2: *The action–angle coordinates of the symmetric Euler–Poinsot system.*

a chart singularity, which conceptually can be ignored.[4] The singularity $m \times e_3$ of the action–angle variables, instead, reflects a substantial fact: going to the border of M, the two–dimensional tori shrink to circles, corresponding to proper rotations. Such a singularity must be taken into serious account in the study of giroscopic motions. The theoretical study needs care, and requires the use of other local coordinates, namely cartesian–like ones, see below.

B. Normal forms. In ref. [3], [4] the system (1.1) was studied within Nekhoroshev theory, respectively for non gyroscopic and for gyroscopic motions. We shall treat here non gyroscopic motions; for an account of the theory for the case of gyroscopic motions, see Section 4. The perturbation study requires the decomposition of the action space A into resonant and nonresonant regions, according (as usual) to the arithmetic properties of ω. Given any $\nu = (\nu_1, \nu_2) \in \mathbb{Z}^2$, the ν–resonant manifold, or line, is the line $\omega(G, L) \cdot \nu = 0$. Introduce then a cutoff

$$N(\varepsilon) \sim \varepsilon^{-1/4} \ ,$$

and consider only the resonant lines of "order" $|\nu| = |\nu_1| + |\nu_2|$ smaller than $N(\varepsilon)$.

A motion is regarded as (approximately) "resonant" with $\nu \in \mathbb{Z}^2$, $|\nu| \le N(\varepsilon)$, if (G_0, L_0) lies within a distance of order $\varepsilon^{1/4}/|\nu|$ from the ν–resonant line. A motion with initial datum which is not resonant with any ν, up to $N(\varepsilon)$, is instead regarded as "nonresonant". The idea behind the introduction of the cutoff (as is typical of Nekhoroshev theory) is that, because of the exponential decay of the Fourier harmonics of analytic functions, the dynamical effect of a resonance ν manifests itself on times of the order $\exp|\nu|$; so for resonances of order larger than the cutoff, this time is longer than the Nekhoroshev time $\exp \varepsilon^{-1/4}$ on which we consider the system.

As proved in [3], the dynamics of a nonresonant motion is described by a normal form Hamiltonian of the type

$$\mathcal{H}' \ = \ \mathcal{K}(G', L') \ + \ \varepsilon \mathcal{W}(G', L', J', j') \ + \ O(\exp - \varepsilon^{-1/4}) \, , \tag{2.1}$$

where $\mathcal{W} = \overline{\mathcal{V}} + O(\varepsilon^{1/4})$, the bar denoting the average over the two fast angles g, l; the distance between the old (unprimed) and the new (primed) variables is of order $\sqrt{\varepsilon}$. This normal form leads to the exponential estimates mentioned in the Introduction. Indeed, the two actions G' and L' stay

[4]The related difficulty is overcome, in the theoretical study, by covering M by two charts of action–angle coordinates, relative to two spatial frames with different z–axis; as proven in [9], the resulting perturbation scheme turns out to be chart independent.

nearly constant for times of the order of $\exp \varepsilon^{-1/4}$, and consequently, for the energy conservation, $\mathcal{W}(G', L', J', j')$ stays also nearly constant. Passing to the old variables, it turns out that G and L stay constant up to $\sqrt{\varepsilon}$, while the function on the sphere

$$\widehat{\mathcal{V}}(J,j) := \overline{\mathcal{V}}(G_0, L_0, J, j)$$

is such that

$$\left|\widehat{\mathcal{V}}(J_t, j_t) \;-\; \widehat{\mathcal{V}}(J_0, j_0)\right| \;\le\; \text{const}\, \varepsilon^{1/4} \ ,$$

still for $|t| < \exp \varepsilon^{-1/4}$. This means that, for the whole exponential time scale, the tip of the unit vector μ in the direction of m remains near a level curve of a function on the unit sphere. So, as claimed, the motion of the angular momentum in space is essentially one–dimensional and ordered (hyperbolic points and irregular motions are allowed, but only in thin strips which shrink to lines for small ε).

For approximately resonant motions, instead, one can only construct a resonant normal form. The new Hamiltonian has still the form (2.1), but now the function $\mathcal{W}$ is obtained by averaging out only one angle, namely a convenient "fast" linear combination ϕ of g and l, while the "slow" angle $\sigma = \nu_1 g + \nu_2 l$ is not eliminated and appears among the arguments of $\mathcal{W}$. The above illustrated mechanism of confinement of μ breaks, and it gets possible that the degree of freedom (J,j) effectively interacts with the slow degree of freedom (S,σ), S being the linear combination of G and L conjugate to σ. In other words, even if the exponentially small remainder is neglected, one is left with a two–degrees of freedom Hamiltonian $\mathcal{K} + \varepsilon\mathcal{W}$, which might be chaotic.

Specifically, after neglecting the remainder and introducing in the standard way the slow and fast variables (S, F, σ, ϕ), one is left with a Hamiltonian of the form

$$\frac{S^2}{2\mathcal{I}} \;+\; \varepsilon\mathcal{W}(F, S, J', \sigma, j') \ , \qquad \mathcal{I} = \frac{I_1}{\nu_1^2 + \eta\nu_2^2} \ , \tag{2.2}$$

where of course the fast action F plays the role of a parameter (see [3]). From now on, we shall drop the primes on J, j. It is not obvious that for Hamiltonians of this form the two degrees of freedom (S,σ) and (J,j) are effectively coupled, and chaotic motions are present. The point is that the pair (J,j) moves on a time scale $O(\varepsilon)$, while (S,σ), due to the Hamilton equation $\dot\sigma = S/\mathcal{I}$, is faster, unless it is $S = O(\varepsilon)$ for sufficiently long time intervals (such a situation is typical of degenerate systems). As pointed out in [3], an effective interaction is expected when S, σ are made slow, for the presence of hyperbolic points with separatrices (see [7] for a general study of such a situation in a case with one and a half degrees of freedom). In this case, *no matter how small is ε,* there are regions in the phase space of the effective Hamiltonian in which the two degrees of freedom get strongly coupled, and chaotic motions (in particular, motions of the tip of μ filling a genuine two–dimensional region) become possible. In [3], this possibility was illustrated by numerically integrating a sample Hamiltonian of the form (2.2), which however was not obtained, through averaging, from a rigid body Hamiltonian. In this paper instead we investigate the possible presence of chaotic motions directly in the dynamics of the rigid body.

Remark: The search for slow chaos should be addressed to low order resonances alone. Indeed, as pointed out in [12], slow chaos cannot take place in resonances of high order $|\nu| \sim \log \varepsilon^{-1}$.

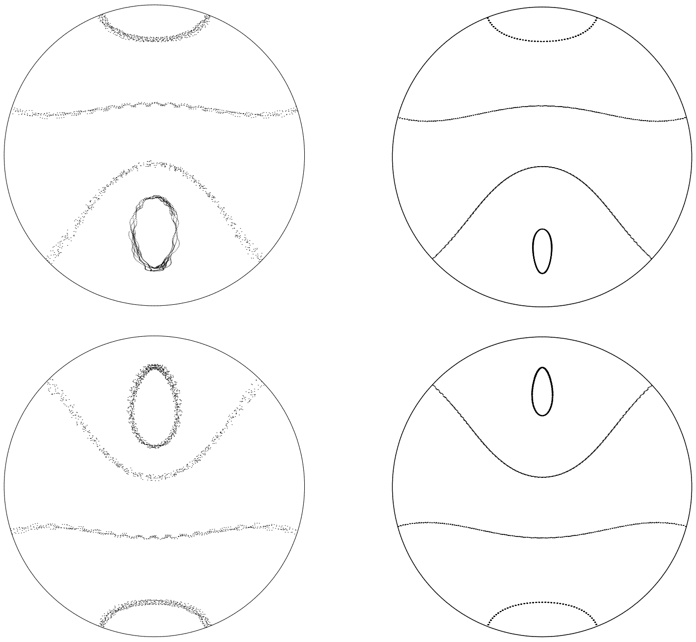

Figure 3: *Nonresonant motions for the potential* V_1*, for* $\varepsilon = 2 \times 10^{-2}$ *(left) and* $\varepsilon = 2 \times 10^{-3}$ *(right); integration times respectively* 10^6 *and* 10^7*. Polar stereographic projection, "north" emisphere up.*

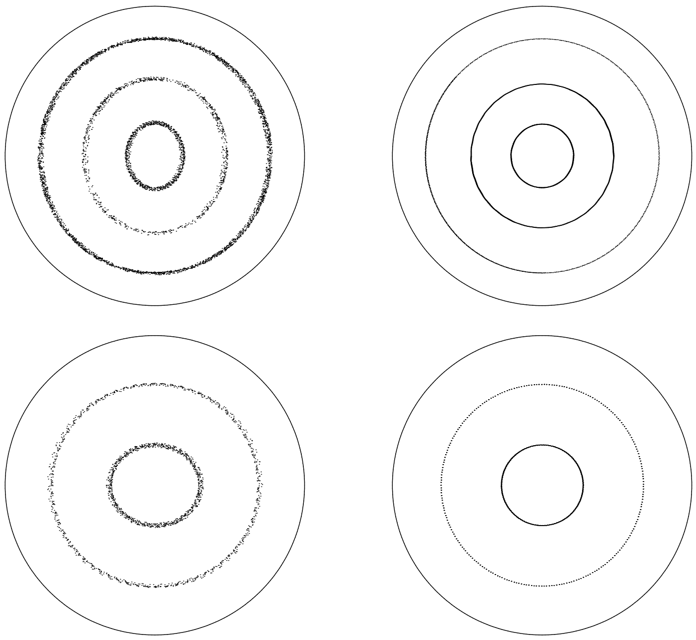

Figure 4: *Nonresonant motions for the potential* V_2*, for* $\varepsilon = 2 \times 10^{-2}$ *(left) and* $\varepsilon = 2 \times 10^{-3}$ *(right); integration times respectively* 10^6 *and* 10^7*.*

3 Results for non–gyroscopic motions

After some trials, we focused the attention on three simple potentials $\mathcal{V}_1$, $\mathcal{V}_2$ and $\mathcal{V}_3$, which in Euler angles are given by[5]

$$\begin{aligned} V_1(\theta,\phi,\psi) &= \sin\theta\cos\phi + \sin^2\theta\cos^2\psi \\ V_2(\theta,\phi,\psi) &= \sin^2\theta\sin\phi\sin\psi + \cos\theta \\ V_3(\theta,\phi,\psi) &= V_1(\theta,\phi,\psi) + V_2(\theta,\phi,\psi) \ . \end{aligned}$$

In action–angle coordinates the potentials turn out to be Fourier polynomials of the angles; their expression, together with the formulae relating the Euler and the action–angle coordinates, can be found in the Appendix.

All computations that we are going to describe have been performed with $\omega(G_0, L_0)$ of order one, more precisely with $I_1 = 1$ and $G_0 = 1$ (this fixes the time scale in the system); the time step was typically $\tau = 0.05$, occasionally smaller. Integration times, indicated in the figure captions, grow proportionally to ε^{-1} (slow chaos is indeed expected to possibly develop on a time scale proportional to ε^{-1}), and are typically between $10^4\varepsilon^{-1}$ and $5\times10^4\varepsilon^{-1}$. In the figures we plot the position of the tip of the unit vector $\mu = m/\|m\|$ on the unit sphere, at equal time intervals. This choice differs of course from the standard Poincaré section procedure used for studying chaotic motions, and is motivated both by the high dimensionality of the problem and by the fact that, in our problem, the significant object is precisely the size of the region visited by μ on the unit sphere. To represent graphically the sphere we use the common polar stereographic projection ("north" hemisphere up).

Nonresonant motions. Figure 3 refers to potential V_1 and nonresonant initial data, more precisely to $\eta = 2$, $G_0 = 1$, $L_0 = 0.314$. The left and right parts of the figure refer respectively to $\varepsilon = 2\times10^{-2}$ and $\varepsilon = 2\times10^{-3}$; for each value of ε, five orbits, differing for the initial values of J and j, are represented, the initial data being the same for the two values of ε. Quite clearly, by decreasing ε all motions shrink to lines, and it would be easy to check that such lines coincide, within great accuracy, with the level lines of the averaged potential. Figure 4 is the same as figure 3, for the potential V_2 (same values of ε and same initial values of the actions G, L). For this potential, it turns out (see the Appendix) that the average of $\mathcal{V}_2$ on g and l is independent of j, and correspondingly the motions of μ on the unit sphere are confined, for small ε, to the parallels of the sphere.

Resonant motions. The search for chaotic behaviour in resonance, which is the central aim of the work, is a delicate matter. Indeed, as already remarked, in principle it would be necessary to show that slow chaos exists for no matter how small ε, on time scales growing as ε^{-1}, and this is numerically costly. Practically, we have been able to observe chaotic motions of μ on the unit sphere, filling a two dimensional portion of it which does not reduce to a line for small ε, for all of the three above potentials, in several low resonances, with ε down to, in some cases, 10^{-6}.

Figure 5 refers to the potential V_2, and shows just one chaotic orbit for $\varepsilon = 10^{-3}$, 10^{-4}, 10^{-5} and 10^{-6}; since the orbit is confined in the upper emisphere, only this is represented. The figure refers

[5] As already remarked, for the numerical integration it is also necessary to consider a second chart of Euler angles, relative to a different spatial frame: for example (as we did) the frame (O, e'_x, e'_y, e'_z) with $e'_x = e_z$, $e'_y = e_x$, $e'_z = e_y$. But this is a technical point, which at a conceptual level can be forgotten. The superscript (i) previously used to distinguish the different representatives of the potential in the different Euler angles charts has been dropped.

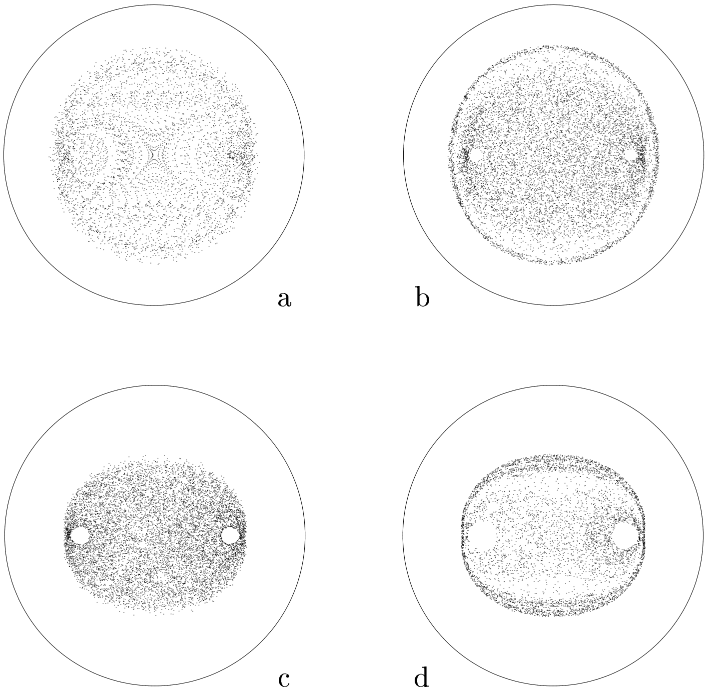

Figure 5: *Motions near the resonance* $(1,-1)$*, for the potential* V_2*, with* $\eta = 2$*, initial values* $(G,L) = (1,0.5)$*,* $\varepsilon = 10^{-3}$ *(a),* 10^{-4} *(b),* 10^{-5} *(c),* 10^{-6} *(d). Only the upper emisphere is represented. Integration times, in the order:* 5×10^7, 5×10^8, 5×10^9, 2.9×10^{10}.

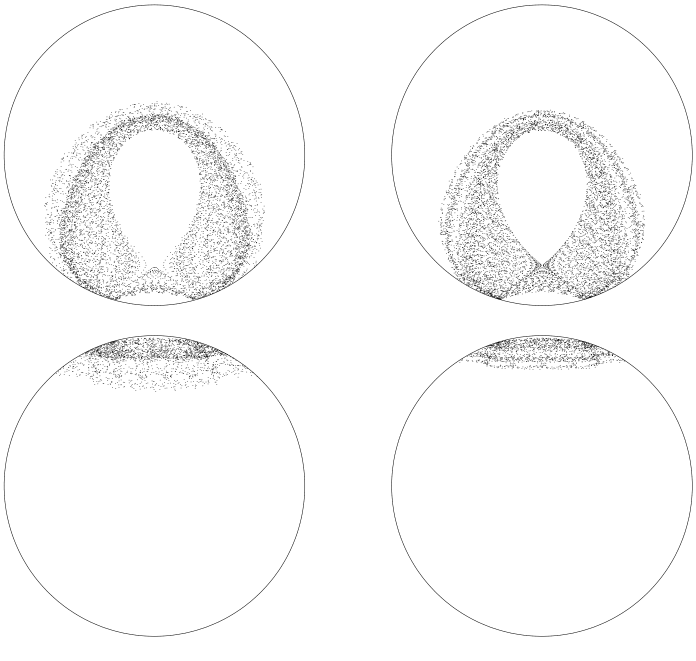

Figure 6: *One chaotic orbit for the potential* V_3*, inside the resonance* $(1,-2)$*, with* $\eta = 2$*,* $(G,L) = (1,0.25)$*;* $\varepsilon = 10^{-3}$ *(left) and* 10^{-4} *(right); integration time respectively* 10^7 *and* 10^8.

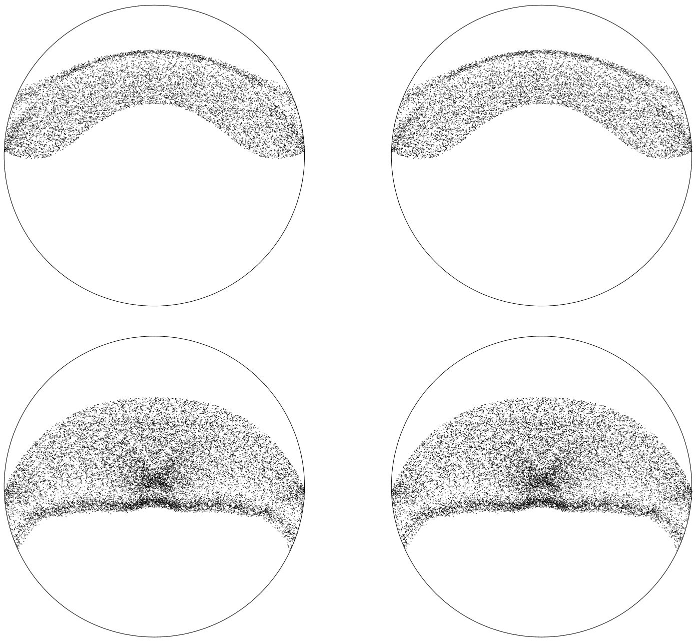

Figure 7: *Same as in figure 6, for different initial* (J, j)*; integration times* 3×10^7 *and* 3×10^8*.*

to $\eta = 2$, resonance $(1, -1)$, initial data $(G, L) = (1, 0.5)$. Although the figures at different ε are not identical,[6] it is clear that the behavior is substantially different from the previous nonresonant case, and a large chaotic region persists, as is theoretically suggested, for the lowest values of ε. The integration time for $\varepsilon = 10^{-6}$ was approximately 3×10^{10}; with $\tau = 0.05$, this corresponds to approximately 6×10^{11} time steps. Increasing significantly the integration time, as it would be necessary to further decrease ε for example to 10^{-7}, appeared prohibitive for our means. Figures 6–9 refer to the potential V_3, with $\eta = 2$. More precisely, figure 6 and 7 show two different chaotic motions inside the same resonance $(1, -2)$, at $\varepsilon = 10^{-3}$ (left) and 10^{-4} (right). The two orbits differ only for the initial choice of (J, j), while for both it was, initially, $(G, L) = (1, 0.25)$. Figure 8 and 9 refer respectively to the resonances $(1, -1)$ and $(1, 2)$, with ε as above.

The conclusion seems to be that slow chaos does exist, as theoretically expected, on a time scale growing by decreasing ε. Not all motions inside resonances are chaotic: by changing the initial data it is easy to find also regular motions, namely motions shrinking to lines for small ε, as the nonresonant ones. The above chaotic motions have been found after some trials.

Normal form analysis. As a further check of good correspondence between theoretical analysis and numerical results, it is interesting to study the normal forms of the Hamiltonians we are dealing with, and check that the dynamics of the normal form, truncated at the lowest order in ε, gives the same motion as the rigid body dynamics, if the initial data are the same and, of course, the considered normal form is adapted to the resonance properties of the initial data. We considered in particular the potential V_1, in the resonance $(1, 2)$, using $\eta = 1$. The second order resonant normal

[6]This is a difference from nondegenerate systems. Indeed, resonant chaotic motions of nondegenerate systems are known to obey precise scale laws for decreasing ε, see for example [5]; the mechanism leading to the scaling, however, breaks down for degenerate systems.

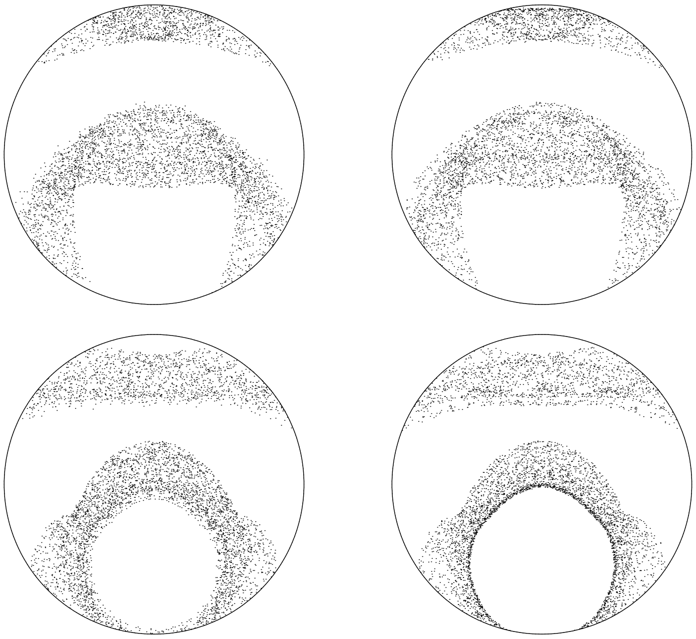

Figure 8: *Same as in figure 6, but in the resonance* $(1,-1)$*; integration times* 10^7 *and* 10^8.

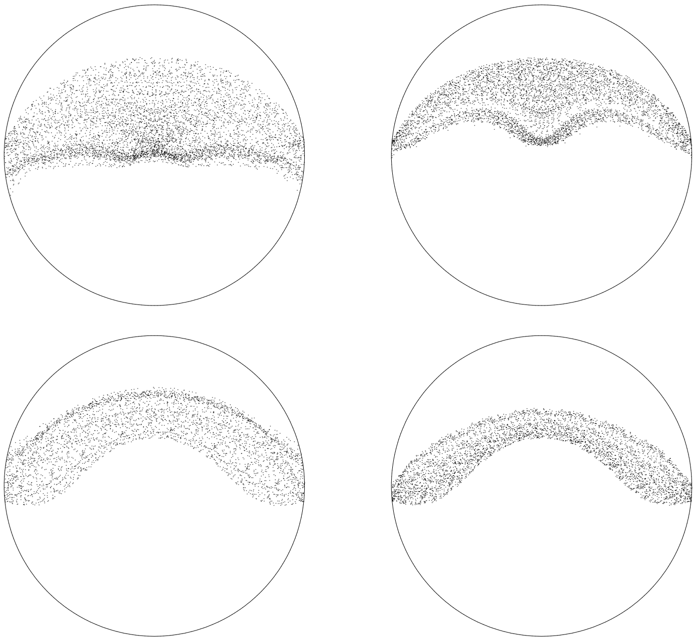

Figure 9: *Same as in figure 6, but in the resonance* $(1,2)$*; integration times* 10^7 *and* 10^8.

form for this potential, in the action–angle coordinates, turns out to be (see the Appendix)

$$\frac{1}{2I_1}\Big(G^2+L^2\Big) \quad + \quad \varepsilon\Big[\frac{J^2}{2G^2}\Big(1-\frac{L^2}{G^2}\Big)+\frac{1}{4}\Big(1+\frac{L^2}{G^2}\Big)\Big(1-\frac{J^2}{G^2}\Big)+\frac{L}{G}\sqrt{1-\frac{J^2}{G^2}}\cos j$$
$$+\frac{1}{2}\frac{J}{G}\Big(1+\frac{L}{G}\Big)\sqrt{1-\frac{L^2}{G^2}}\sqrt{1-\frac{J^2}{G^2}}\cos(g+2l)\Big]\ . \tag{3.1}$$

The 'fast' and 'slow' coordinates (F,S,φ,σ), for the resonance $\nu=(1,2)$, are

$$F=2G-L\,,\qquad S=G-L\,,\qquad \varphi=g+l\,,\qquad \sigma=-g-2l\ ;$$

since the truncated normal form does not depend on the fast angle φ, the fast action F is regarded as a parameter in the foregoing analysis. The resonant line $G=-2L$ has equation $S=S^*(F)=\frac{3}{5}F$, and it is convenient to shift the origin of the slow action to S^*, by the trivial substitution $s=S-S^*(F)$. In the variables (s,J,σ,j), the resonant normal form, further truncated to the first order in s/F (which inside the resonance is as small as $\sqrt{\varepsilon}$), finally becomes

$$\frac{5}{2}s^2+\frac{\varepsilon}{16}\frac{J^2}{G^2}-\frac{\varepsilon}{2}\sqrt{1-\frac{J^2}{G^2}}\Big(\cos j-\frac{\sqrt{3}}{4}\frac{J}{G}\cos\sigma\Big)\ ,$$

where $G=F-S^*(F)$. This is a two–degrees of freedom Hamiltonian and the computation of its dynamics is not difficult, up to the fact that, exactly as for the rigid body, there are chart singularities at $J/G=\pm1$. The way out is the same: considering a second set of action–angle coordinates, repeating in this chart the construction of the normal form and the truncation (both operations commute with the change of chart), using a splitting algorithm.[7] Figure 10, left part, shows a chaotic motion of μ on the unit sphere, as obtained by integrating the normal form; the right part of the figure shows instead the corresponding motion of the rigid body. The similarity of the two images looks satisfactory. Both figures refer to $\varepsilon=10^{-3}$.

As commented above, a numerical study of a Hamiltonian similar to the above normal form was performed in [3]; the essential point added here is that the normal form now comes from a real rigid body problem, through averaging and truncation. Moreover, here we put in evidence the good correspondence between the motions of the lowest order normal form and those of the original rigid body Hamiltonian, which is at the basis of the theoretical interpretation.

4 Gyroscopic motions

Numerical results. Motions with the angular momentum nearly aligned to the symmetry axis are of obvious special interest. They were studied in [4], where it was proved that essentially all the conclusions valid for general motions apply to this case, too (with minor improvements of certain estimates). The analysis of [4] did not put into evidence any mechanism which would lead to expect better regularity properties of nearly gyroscopic motions, as compared to all other motions. Our numerical investigations suggest instead a rather different situation: the difference

[7]A convenient splitting is $\Phi^{H_3}_{\tau/2}\circ\Phi^{H_2}_{\tau/2}\circ\Phi^{H_1}_{\tau}\circ\Phi^{H_2}_{\tau/2}\circ\Phi^{H_3}_{\tau/2}$, with

$$H_1=\frac{5}{2}s^2+\frac{\varepsilon}{16}\frac{J^2}{G^2}\ ,\qquad H_2=-\frac{\varepsilon}{2}\sqrt{1-\frac{J^2}{G^2}}\cos j\ ,\qquad H_3=\varepsilon\frac{\sqrt{3}}{8}\frac{J}{G}\sqrt{1-\frac{J^2}{G^2}}\cos\sigma\ .$$

Indeed it is easy to integrate analitically each of the threee flows, so that the algorithm is explicit.

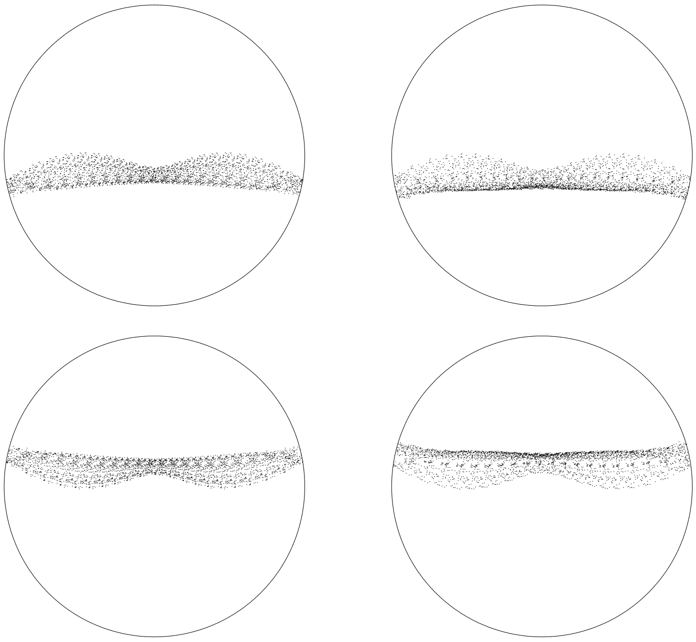

Figure 10: *A chaotic motion of the truncated normal form, for potential* V_1, $\eta = 1$, *resonance* $(1,2)$, $\varepsilon = 10^{-3}$ *(left). The corresponding motion of the rigid body (right). Integration time* 2×10^6.

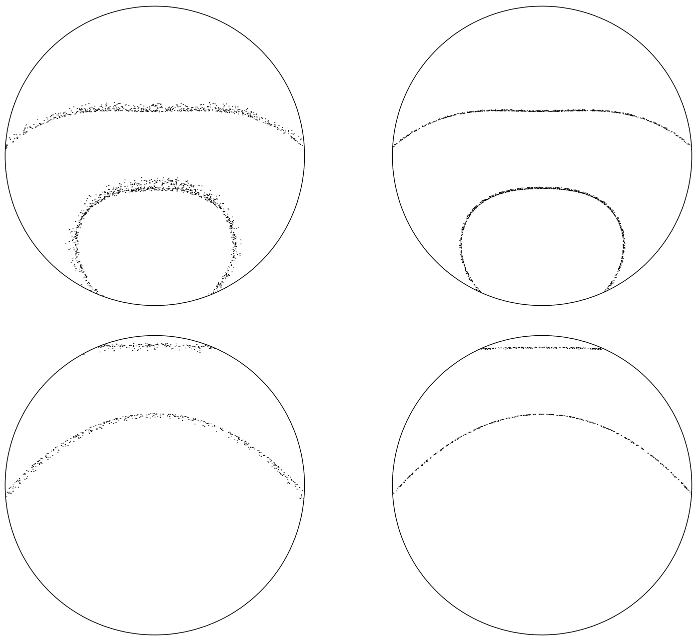

Figure 11: *Resonant gyroscopic motions for the potential* V_3, $\eta = 1$, $(L, G) = (1, -1)$; $\varepsilon = 10^{-2}$ *(left),* 10^{-3} *(right). Integration times respectively* 10^6 *and* 10^7.

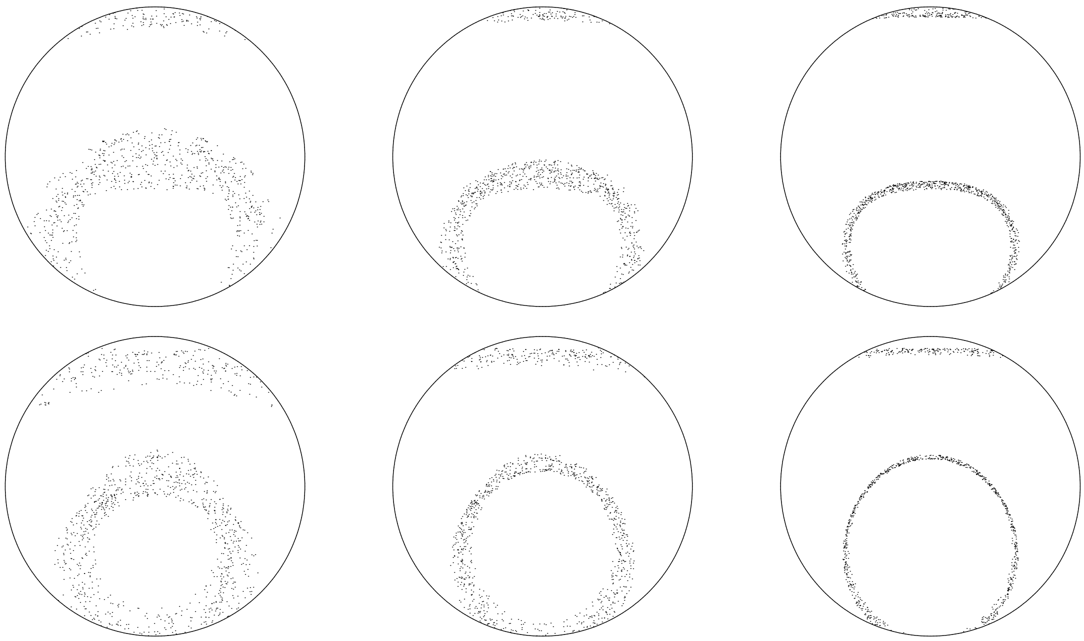

Figure 12: *Resonant motions for the potential* V_3*, at fixed* $\varepsilon = 10^{-3}$*, resonance* $(1,-1)$*, and (left to right)* $\eta = 1.5,\ 1.2,\ 1.05$ *(also compare, for* $\eta = 1$*, with the right part of figure 11). Integration time* 10^7*.*

between resonant and nonresonant motions, which was essential in the non–gyroscopic case, in the gyroscopic case apparently disappears, all motions becoming regular by decreasing ε. We made a careful search of slow chaotic motions among nearly gyroscopic ones, but we never detected any of them.

A typical situation is illustrated in figure 11. The figure refers to the potential V_3, in the resonance $(1,-1)$; the resonant line is $G - \eta L = 0$, and the gyroscopic condition $L = G$ is obtained for $\eta = 1$. The figure shows two resonant motions, each for two values of ε, namely $\varepsilon = 10^{-2}$ (left) and 10^{-3} (right). Quite clearly, the motions of μ fill thin two–dimensional regions for the larger value of ε, but, precisely as in the previous case of nonresonant motions, such regions narrow to curves when ε is reduced. Figure 12 confirms this situation in a complementary way: now $\varepsilon = 10^{-3}$ is fixed, while η is changed so as to push the resonant line to the gyroscopic situation $L = G$. The three parts of the figure refer (left to right) to $\eta = 1.5,\ 1.2,\ 1.05$; also compare, for $\eta = 1$, with the right part of figure 11 (one of the orbits has been there changed, to have a strip of nonvanishing width at $\varepsilon = 10^{-2}$). Quite clearly, by approaching the gyroscopic rotations chaotic motions progressively disappear. Finally, figure 13 refers to the resonance $(1,2)$, $\eta = -\frac{1}{2}$. Such a resonance is somehow exceptional, since it cannot be approached by moving η (indeed for $\eta > -\frac{1}{2}$ the resonance condition $G + 2\eta L = 0$ gives $L > G$, so the resonant line is out of the action space), but according to the theory, see below, it is the most promising one: in this case too, however, by decreasing ε chaotic motions disappeared. In the figure we report (left to right): $\varepsilon = 10^{-2}$, $\varepsilon = 10^{-3}$, $\varepsilon = 10^{-4}$. Integration times (see the captions) as usual grow with ε^{-1}, and are of the same order as the times at which, out of the gyroscopic condition, slow chaos manifestly appears.

These results clearly suggest that gyroscopic motions have stronger long–time stability properties than all other motions. This conclusion is perhaps not surprising, because it agrees with the common expectation and the everyday–experience, but mathematically it needs to be explained.

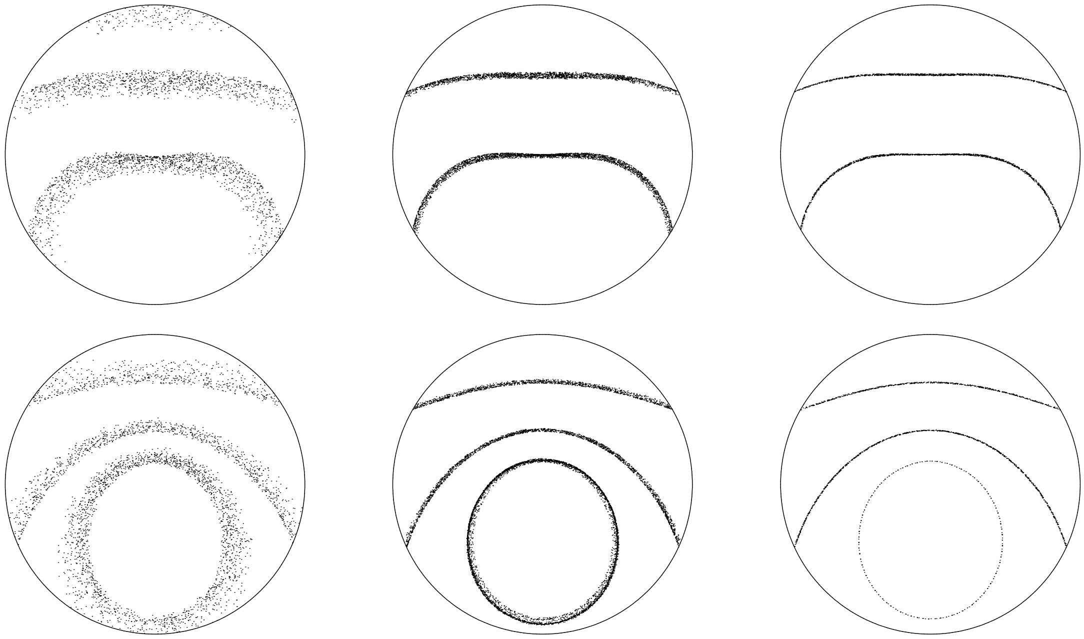

Figure 13: *Resonant gyroscopic motions for the potential* V_3*, resonance* $(1,2)$*;* $\eta = -0.5$, $(L,G) = (1,1)$ *and (left to right)* $\varepsilon = 10^{-2}$, 10^{-3}, 10^{-4}*. Integration times, in the order,* 2×10^6, 2×10^7, 2×10^8.

The results of [4] go in the right direction, but are not sufficient, and a substantial improvement looks necessary. We plan to devote to this problem a future work, since it requires an appropriate theoretical setting and some technicism; here we limit ourselves to only a few comments toward a possible explanation.

Discussion. Nearly gyroscopic motions cannot be studied by using the action–angle coordinates, because of their singularity. Instead, one can use coordinates (G,γ,x_1,x_2,J,j), where the angle γ is defined as $g+l$ on nongyroscopic motions and as the Eulerian angle ψ on gyroscopic motions, and

$$x_1 = \sqrt{2\Lambda}\cos\lambda\,, \quad x_2 = -\sqrt{2\Lambda}\sin\lambda\,,$$

with $\Lambda = G-L$, $\lambda = -l$ (see e.g. [4]). These coordinates still retain the singularity at $J=\pm G$, but this is a technical problem, which is overcome in [4] by using a two–charts atlas with these coordinates, and conceptually it can be ignored.

As is customary in perturbation theory, in place of (x_1,x_2) it is convenient to use the complex coordinates $z=(z_1,z_2)$ defined by

$$z_1 = \frac{x_1 - ix_2}{i\sqrt2}\,, \qquad z_2 = \frac{x_1+ix_2}{\sqrt2}\,.$$

Though Λ is not a coordinate, but a function on the phase space, it is nevertheless useful to take into consideration the action space $A = \{(G,\Lambda) : |\Lambda| \le G\}$, since the kinetic energy and the frequencies of the Euler–Poinsot system depend only on G and Λ.

Regarded as a function on the action space, the kinetic part of the Hamiltonian becomes

$$\mathcal{K}(G,\Lambda) \;=\; \frac{1}{2I_3}(G^2+\beta\Lambda^2-2\beta G\Lambda)\,, \qquad \beta = 1-\frac{I_3}{I_1} = \frac{\eta}{\eta+1}\;;$$

note that $-1 \le \beta \le 1$ and that $\beta = -1$ for a flat body, $\beta = 0$ for a spherical body, $\beta = 1$ for a linear body. We exclude from our consideration the cases of linear and spherical bodies, which should be studied separately.

We shall denote by $\Omega(G,\Lambda) = (G-\beta\Lambda, -\beta G+\beta\Lambda)$ the frequency vector in these coordinates; the relation with the frequency ω in the previous coordinates is $\Omega = (\omega_1+\omega_2, -\omega_2)$, and correspondingly, if $\nu \in \mathbb{Z}^2$ resonates with ω, then $N = (\nu_1, \nu_1 - \nu_2)$ resonates with Ω. On the gyroscopic motions it is

$$\Omega(G,0) \ = \ G\,(1,-\beta) \ ,$$

so a gyroscopic rotation is exactly resonant with N if $N_1 = \beta N_2$. This however requires $|N_1| \le |N_2|$, and so, excluding the cases of linear and spherical bodies, the resonance of lowest order is $N = (1,-1)$, which is met when $\beta = -1$ (flat body), followed by $N = (\pm 1, 2)$, $(\pm 1, 3)$, $(\pm 2, 3)$ etc. The resonance $N = (-1, 1)$ corresponds to $\nu = (1, 2)$, and is the one considered in figure 13; the resonance $N = (1, 2)$ corresponds to $\nu = (1, -1)$ and is the one considered in figures 11 and 12.

The importance of the order $|N| = |N_1| + |N_2|$ is understood by writing down the resonant normal forms. To this end, we need to introduce a little bit of notations (see [4] or [11] for motivations and further details). Let

$$f(G,\gamma,z_1,z_2,J,j) \ = \ \sum_{N_1\in\mathbb{Z}} \ \sum_{m,n\in\mathbb{N}} f_{N_1,m,n}(G,J,j)\, e^{iN_1\gamma}\, z_1^m z_2^n$$

be the expansion of a function f in Taylor series around $z = 0$ and in Fourier series in the angle γ. An expansion of f which is precisely the Fourier series in the angles γ and λ, written however using (z_1, z_2) in place of (Λ, λ) so as to avoid the singularity $\Lambda = 0$, is the less fragmented expansion

$$f \ = \ \sum_{N\in\mathbb{Z}^2} f_N \ ,$$

where for any $N \in \mathbb{Z}^2$ the N–th *harmonic* f_N of f is defined as

$$f_N(G,\gamma,z_1,z_2,J,j) \ = \ \sum_{\substack{m,n\in\mathbb{N}\\ m-n=N_2}} f_{N_1,m,n}(G,J,j)\, e^{iN_1\gamma}\, z_1^m z_2^n \ ;$$

note that out of the singularity it is $z_1^m z_2^n = (-i)^m \Lambda^{\frac{1}{2}(m+n)} e^{iN_2\lambda}$. Quite clearly, for nonvanishing N_2 the harmonics f_N is divisible either by $z_1^{N_2}$ or by $z_2^{-N_2}$, depending on whether N_2 is positive or negative. Therefore, as long as $N_2 \ne 0$, f_N becomes small near the gyroscopic rotation—the smaller the bigger is $|N_2|$.

Assume now that the gyroscopic rotation is resonant with a given vector $N = (N_1, N_2)$, so that $N_1 = \beta N_2$, with relative prime numbers N_1 and N_2. In this case, one can construct a resonant normal form in the vicinity of the gyroscopic rotation, which has the form

$$\mathcal{K} + \varepsilon \mathcal{W} + O(\exp -\varepsilon^{-1/4}) \ , \qquad (4.1)$$

the function $\mathcal{W}$ having nonzero harmonics $\mathcal{W}_{N'}$ only for $N' = nN$, $n \in \mathbb{Z}$, that is

$$\mathcal{W} \ = \ \sum_{n\in\mathbb{Z}} \mathcal{W}_{(nN_1,nN_2)}(G,z_1,z_2,J,j)\, e^{inN_1\gamma} \, .$$

The γ–dependence of $\mathcal{W}$ can be eliminated by passing to the corotating coordinates $(\Gamma, \gamma, w_1, w_2, J, j)$, where

$$\Gamma \ = \ G - \beta\Lambda \, , \qquad w_1 \ = \ e^{i\beta\gamma} z_1 \, , \qquad w_2 \ = \ e^{-i\beta\gamma} z_2 \, ,$$

which are the analog of the slow and fast actions. Observing also that the average $\mathcal{W}_0$ of $\mathcal{W}$ does not depend on z_1 and z_2 separately, but only on $\Lambda = iz_1z_2$, one concludes that the normal form Hamiltonian (4.1) has the form

$$\mathcal{K}(G,\Lambda) + \varepsilon \mathcal{W}_0(G,\Lambda,J,j) + \varepsilon \widehat{\mathcal{W}}(G,w_1,w_2,J,j) + O(\exp -\varepsilon^{-1/4}) \ ,$$

where G stands now for $\Gamma + \beta\Lambda = \Gamma + i\beta w_1 w_2$. Here the quantity $\widehat{\mathcal{W}} = \mathcal{W} - \mathcal{W}_0$ is of order $\Lambda^{|N_2|/2}$ and so, for $|N_2| \geq 2$, the normal form can still be regarded as a small perturbation of the integrable system $\mathcal{K} + \varepsilon\mathcal{W}_0$ (which would produce motions of μ on curves in the unit sphere), the new additional small parameter being the distance from the gyroscopic rotation. *This is the crucial fact, which was not taken into account in* [4].

It should be therefore expected that no chaotic behaviour take place, on times which grow exponentially fast with the inverse of the initial distance from the gyroscopic rotations. Proving this fact requires a careful technical analysis, that we leave to a dedicated work.

The case $N_2 = 1$ is special, since the harmonics $\mathcal{W}_N$ may have nonzero terms which are linear in z_1 and z_2. In such a case, the Hamiltonian vector field of this harmonic does not vanish at $z = 0$, and the above argument alone might be insufficient. In fact, we expected at first that this case might lead to chaotic behaviour. One should note that the only possible resonance with $|N_2| = 1$ (in coordinates (Γ, Λ)) is the resonance $N = (1, -1)$, which is met only in the case of a flat body. Figure 13 arose out of an attempt of finding chaotic motions in this resonance.

5 Appendix: action–angle coordinates

First of all we collect here a few formulas relating the Euler angles (θ, ϕ, ψ) to the action–angle coordinates (G, L, J, g, l, j). Define

$$\begin{aligned}
\Theta(x,y,g) &= xy - \sqrt{1-x^2}\,\sqrt{1-y^2}\,\cos g \\
C(x,y,g) &= \frac{y\sqrt{1-x^2} + x\sqrt{1-y^2}\,\cos g}{\sqrt{1-\Theta(x,y,g)^2}} \\
S(x,y,g) &= \frac{\sqrt{1-y^2}\,\sin g}{\sqrt{1-\Theta(x,y,g)^2}} \ ;
\end{aligned}$$

note that $C(x,y,g)^2 + S(x,y,g)^2 = 1$. Then

$$\begin{aligned}
\cos\theta &= \Theta(\hat{J},\hat{L},g) \\
\sin\theta &= \sqrt{1-\Theta(\hat{J},\hat{L},g)^2} \\
\begin{pmatrix}\cos\varphi \\ \sin\varphi\end{pmatrix} &= \begin{pmatrix} C(\hat{J},\hat{L},g) & -S(\hat{J},\hat{L},g) \\ S(\hat{J},\hat{L},g) & C(\hat{J},\hat{L},g)\end{pmatrix} \begin{pmatrix}\cos j \\ \sin j\end{pmatrix} \\
\begin{pmatrix}\cos\psi \\ \sin\psi\end{pmatrix} &= \begin{pmatrix} C(\hat{L},\hat{J},g) & -S(\hat{L},\hat{J},g) \\ S(\hat{L},\hat{J},g) & C(\hat{L},\hat{J},g)\end{pmatrix} \begin{pmatrix}\cos l \\ \sin l\end{pmatrix}
\end{aligned}$$

where $\hat{J}$ and $\hat{L}$ stand, respectively, for J/G and L/G. The first two equalities are proven in [3]. The remaining ones are proven by observing that they are equivalent to the four equalities

$\cos(\varphi - j) = C(\hat{J}, \hat{L}, g)$, $\sin(\varphi - j) = S(\hat{J}, \hat{L}, g)$, $\cos(\psi - l) = C(\hat{L}, \hat{J}, g)$ and $\sin(\psi - l) = S(\hat{L}, \hat{J}, g)$; the first and the last of these equalities are proven in [3], while the second and the third are there proven with absolute values, but it is easy to verify that they are in fact correct.

Note that $\cos\theta$ and the products of $\sin\theta$ by either the cosine or the sine of either φ or ψ are trigonometric potentials in the three angles g, l, j; instead, $\sin\theta$ alone is not a trigonometric potential. This is one of the reasons behind the choice of the potentials V_1 and V_2 in Section 3: our aim was indeed to have a good control of the normal forms of the corresponding Hamiltonians, so we choose potentials such that their expression in action–angle coordinates was simple enough.

In action–angle coordinates the potentials V_1 and V_2 assume respectively the form

$$\begin{aligned}\mathcal{V}_1(\hat{L}, \hat{J}, g, l, j) \;=\; & \Big(\hat{L}\sqrt{1-\hat{J}^2} + \hat{J}\sqrt{1-\hat{L}^2}\cos g\Big)\cos j - \sqrt{1-\hat{L}^2}\sin g \sin j \\ & + \Big[\Big(\hat{J}\sqrt{1-\hat{L}^2} + \hat{L}\sqrt{1-\hat{J}^2}\cos g\Big)\cos l - \sqrt{1-\hat{J}^2}\sin g\sin l\Big]^2\end{aligned}$$

and

$$\begin{aligned}\mathcal{V}_2(\hat{L}, \hat{J}, g, l, j) \;=\; & \hat{L}\hat{J} - \sqrt{1-\hat{L}^2}\sqrt{1-\hat{J}^2}\cos g \\ & + \Big[\sqrt{1-\hat{L}^2}\sin g\cos j + \Big(\hat{L}\sqrt{1-\hat{J}^2} + \hat{J}\sqrt{1-\hat{L}^2}\cos g\Big)\sin j\Big] \\ & \times \Big[\sqrt{1-\hat{J}^2}\sin g\cos l + \Big(\hat{J}\sqrt{1-\hat{L}^2} + \hat{L}\sqrt{1-\hat{J}^2}\cos g\Big)\sin l\Big]\;.\end{aligned}$$

The averages on the fast angles, entering the nonresonant normal form, are respectively

$$\begin{aligned}\overline{\mathcal{V}_1} &= \frac{1}{2}\hat{J}^2(1-\hat{L}^2) + \frac{1}{4}(1+\hat{L}^2)(1-\hat{J}^2) + \hat{L}\sqrt{1-\hat{J}^2}\cos j \\ \overline{\mathcal{V}_2} &= \hat{L}\hat{J}\;;\end{aligned}$$

the nonresonant motions represented in figures 3 and 4 shrink, for small ε, to the level lines of these functions (as noticed in Section 3, $\overline{\mathcal{V}_2}$ is independent of j, so for small ε motions shrink to circles).

The resonant harmonics of potential $\mathcal{V}_1$, corresponding to $\nu = (1, 2)$, is easily found to be

$$(\mathcal{V}_1)_{(1,2)} = \frac{1}{2}\hat{J}(1+\hat{L})\sqrt{1-\hat{L}^2}\sqrt{1-\hat{J}^2}\,\cos(g+2l)\;;$$

the second order resonant normal form is then $\mathcal{K}(G, L) + \varepsilon\overline{\mathcal{V}_1} + \varepsilon(\mathcal{V}_1)_{(1,2)}$, and this coincides with (3.1).

References

[1] G. Benettin, A.M. Cherubini and F. Fassò, *A "changing chart" symplectic algorithm for rigid bodies and other dynamical systems on manifolds.* SIAM Journ. Sci. Comp. **23**, 1189–1203 (2001).

[2] G. Benettin and A. Giorgilli, *On the Hamiltonian interpolation of near to the identity symplectic mappings, with application to symplectic integration algorithms.* J. Stat. Phys. **74**, 1117–1144 (1994).

[3] G. Benettin and F. Fassò, *Fast rotations of the rigid body: A study by Hamiltonian perturbation theory. Part I.* Nonlinearity **9**, 137–186 (1996).

[4] G. Benettin, F. Fassò and M. Guzzo, *Fast rotations of the rigid body: A study by Hamiltonian perturbation theory. Part II: Gyroscopic rotations.* Nonlinearity **10**, 1695–1717 (1997).

[5] G. Benettin and G. Gallavotti, *Stability of Motions near Resonances in Quasi Integrable Hamiltonian Systems.* Journ. Stat. Phys. **44**, 293 (1986).

[6] A. Dullweber, B. Leimkuhler and R. McLachlan, *Symplectic splitting methods for rigid body molecular dynamics.* J. Chem. Phys. **107**, 5840–5851 (1997).

[7] Y. Elskens and D.F. Escande, *Slowly pulsating separatrices sweep homoclinic tangles where islands must be small: an extension of classical adiabatic theory.* Nonlinearity **4**, 615–667 (1991).

[8] D.J. Evans, *On the representation of orientation space.* Mol. Phys. **34**, 317–325 (1977).

[9] F. Fassò, *Hamiltonian perturbation theory on a manifold.* Cel. Mech. and Dyn. Astr. **62,** 43–69 (1995).

[10] F. Fassò, *The Euler–Poinsot top: a non–commutatively integrable systems without global action–angle coordinates.* J. Appl. Math. Phys. (ZAMP) **47**, 953–976 (1996).

[11] F. Fassò, M. Guzzo and G. Benettin, *Nekhoroshev–stability of elliptic equilibria of Hamiltonian systems.* Comm. Math. Phys. **197**, 347–360 (1998).

[12] M. Guzzo, *Nekhoroshev stability of quasi–integrable degenerate Hamiltonian Systems.* Regular and Chaotic Dynamics **4**, 78–102 (1999).

[13] M. Guzzo and A. Morbidelli, *Construction of a Nekhoroshev like result for the asteroid belt dynamical system.* Cel. Mech. and Dyn. Astr. **66**, 255–292 (1997).

[14] E. Hairer, *Backward analysis of numerical integrators and symplectic methods.* Ann. Num. Math. **1**, 107–132 (1994).

[15] E. Hairer, *Global modified Hamiltonian for constrained symplectic integrators.* Submitted for publication (2002).

[16] A. Kol, B. Laird and B. Leimkuhler, *A symplectic method for rigid–body molecular simulation.* J. Chem. Phys. **107**, 2580–2588 (1997).

[17] B. Leimkuhler and R. Skeel, *Symplectic numerical integrators in constrained Hamiltonian systems.* J. Comp. Phys. **112**, 117–125 (1994).

[18] R.I. McLachlan, *Explicit Lie–Poisson integration and the Euler equations*, Phys. Rev. Lett. **71**, 3043–3046 (1993).

[19] S. Reich, *Momentum conserving symplectic integrators*, Physica D **76**, 375–383 (1994).

[20] S. Reich, *Symplectic integration of constrained Hamiltonian systems by composition methods.* SIAM J. Numer. Anal. **33**, 475–491 (1996).

[21] S. Reich, *On high–order semi–explicit symplectic partitioned Runge–Kutta methods for constrained Hamiltonian systems.* Numer. Math. **76** 231–247 (1997).

[22] J. Touma and J. Wisdom, *Lie–Poisson integrators for rigid body dynamics in the solar system.* Astr. J. **107**, 1189–1202 (1994).

[23] H. Yoshida, *Construction of higher order symplectic integrators.* Phys. Lett. A **150**, 262–268 (1990).

[24] H. Yoshida, *Recent progress in the theory and application of symplectic integrators.* Cel Mech. and Dyn. Astr. **56**, 27–43 (1993).